Universiteit Antwerpen

This item is the archived peer-reviewed author-version of:

One-step microheterogeneous formation of rutile@anatase coreshell nanostructured microspheres discovered by precise phase mapping

One-step microheterogeneous formation of rutile@anatase core-shell nanostructured microspheres discovered by precise phase mapping

Alexey Tarasov[1,4,†,*], Zhi-Yi Hu[2,†,*], Maria Meledina[2], German Trusov[3], Eugene Goodilin[4], Gustaaf Van Tendeloo[2], Yuri Dobrovolsky[5]

1. Department of Chemistry, Lomonosov Moscow State University; Moscow, Leninskie Gory, 119991, Moscow, Russia

2. EMAT (Electron Microscopy for Materials Science), University of Antwerp, 171 Groenenborgerlaan, B-2020 Antwerp, Belgium

3. National University of Science and Technology, "MISIS", 119049, Moscow, Leninskiy prospect 4, Moscow, Russia

4. Faculty of Materials Science, Lomonosov Moscow State University; Leninskie Gory, 119991, Moscow, Russia

5. Institute of Problems of Chemical Physics RAS, Academician Semenov avenue 1, 142432, Chernogolovka, Russia.

† The authors contributed equally to this work.

* Corresponding author

Abstract

Nanostructured core-shell microspheres with a rough rutile core and a thin anatase shell are synthesized via a one-step heterogeneous templated hydrolysis process of $TiCl_4$ vapor on the aerosol water-air interface. The rutile-in-anatase core–shell structure has been evidenced by different electron microscopy techniques, including electron energy-loss spectroscopy (EELS) and 3D electron tomography. A new mechanism for the formation of a crystalline rutile core inside the anatase shell is proposed based on a statistical evaluation of a large number of electron microscopy data. We found that the control over the $TiCl_4$ vapor pressure, the ratio between $TiCl_4$ and H_2O aerosol, and the reaction conditions plays a crucial role in the formation of the core-shell morphology and increases the yield of nanostructured microspheres.

1. Introduction

Titanium dioxide attracts profound interest as a promising nanomaterial for photovoltaics, water photosplitting, air purification and lithium storage.[1–5] In particular, titania based core-shell materials attract special attention because of their promising applications in photocatalysis.[6,7] Many studies showed that pure anatase is more active in photocatalytic reactions than rutile. However, it is also confirmed that the presence of both phases causes a transfer of photogenerated electrons and holes between the different phases, thus improving the charge separation efficiency and the overall activity of the composite material.[8–11]

Uniform 10 nm rutile nanowires evenly coated by an anatase film and assembled into flower-like 3μm microspheres have been recently prepared by a hydrothermal treatment of a mixed phase TiO_2 powder.[7] Similar structures were obtained by the deposition of anatase on the surface of 200-500 nm rutile microspheres via a vapor phase hydrolysis process.[12] Rutile–anatase nanocrystalline TiO_2 with a core–shell structure was synthesized via a phase conversion method with semicrystalline TiO_2

embedded in a caramelized sucrose matrix, treated hydrothermally, and annealed.[13] Nanowires with a $TiO_2(B)$ core and an anatase shell were grown on titanium foil via a four-step route.[14] Unfortunately, most of the preparation techniques of such core-shell materials are time- and resource-consuming syntheses.

The aerosol pyrolysis technique is known as a facile way to prepare various microspheres with different composition because of the precise spherical shape of aerosol droplets acting as morphology directing agents and isolated microreactors. The pyrolysis of nebulized colloidal solutions in ethanol, containing pre-synthesized Fe_3O_4 particles (future core) and dissolved tetraethyl orthosilicate (TEOS) (future shell) was applied to prepare $Fe_3O_4@C-SiO_2$ core-shell microspheres.[15] Liquid-feed flame spray pyrolysis of an ethanol solution, containing Ce, Zr and Al organic precursors, was used to obtain $(Ce_{0.7}Zr_{0.3}O_2)_x@(Al_2O_3)_{1-x}$ core-shell nanoparticles; this shape was formed due to the difference in vaporization temperature of the different oxides.[16] A single-step pyrolysis of premixed gas precursors in a furnace aerosol reactor was developed to synthesize silica-coated iron oxide nanocomposite materials.[17] Cubic single-crystal NaCl inside hexagonally ordered mesoporous silica spheres were obtained by aerosol pyrolysis of a complex water-based homogeneous precursor containing HCl, cetrimonium bromide (CTAB), NaCl and methyltriethoxysilane/orthosilicate (MTES/TEOS) in ethanol.[18] Spherical submicron-particles with a TiO_2 core and a RuO_2 shell structure were synthesized by employing sequential ultrasonic spray pyrolysis.[19] However, a one-step synthesis of titania-titania core-shell microspheres composed of different TiO_2 phases has not been developed so far.

Recently, a new pyrolysis technique for the preparation of N-doped TiO_2 microspheres with a core-shell structure containing both anatase and rutile phases via heterogeneous $TiCl_4$ vapor hydrolysis using water solution aerosols has been reported.[20,21] However, the internal structure and distribution of anatase and rutile in the core-shell microspheres remains unclear due to the restriction of the characterization techniques. This paper sheds light on the core-shell morphology

and suggests a different formation mechanism of these promising materials. Transmission electron microscopy (TEM) is an ideal tool to investigate both the structure and the chemical composition of multicomponent nanomaterials, using a combination of high-resolution TEM, high-angle annular dark-field scanning transmission electron microscopy (HAADF-STEM), energy dispersive X-ray spectroscopy (EDX) mapping, and electron energy-loss spectroscopy (EELS).[22] With the use of a monochromator, high-resolution energy filters, and an improved mechanical and electrical stability, an energy resolution of around 100meV becomes available in EELS. The hybrid structure of anatase/rutile can therefore be reliably diagnosed through a high-resolution EELS analysis, and the differences in the Ti $L_{2,3}$ edge between anatase and rutile can be detected.[23,24] Equally important, the internal structure can be revealed by electron tomography using 3D reconstruction.[25–30] It allows us to map the distribution of anatase and rutile and image the internal structure of the as-synthesized core-shell microspheres by advanced TEM. Based on our TEM data, we discuss new features of the formation mechanism of microspheres with a rutile@anatase structure and the influence of the synthesis conditions on the particle morphology and the doping features. It was discovered that the occurrence of $TiCl_4$ hydrolysis on the water-air interface defines the core-shell morphology of the TiO_2 microspheres. The proposed preparation technique allows one to tune up simultaneously the doping and the morphological parameters of the titania microspheres. This is important for future scaling up the production using aerosol techniques.

2. Results and discussion

The titania microspheres were synthesized by heterogeneous $TiCl_4$ vapor hydrolysis. Figure 1(a) illustrates the schematic synthesis strategy. Briefly, the flow of $TiCl_4$ vapor and the flow of water based aerosol mix in the T-piece tube leading to the heterogeneous $TiCl_4$ hydrolysis on the surface and inside the aerosol droplets followed by the dehydration and calcination of the hydrolysis products in

the pre-heated tube furnace (1000 $^{\circ}$C). The concentration of $TiCl_4$ in the flow is defined by the temperature of the $TiCl_4$ liquid in the evaporator (70 – 110 $^{\circ}$C). A scanning electron microscopy (SEM) image of the product is shown in Figure 1(b): the resulting microspheres are 0.5–3 µm in diameter and demonstrate a smooth surface. To investigate the inner structure of the microspheres TEM techniques are used. Particularly, in the HAADF-STEM mode, also known as Z-contrast imaging, the scattered intensity is approximately proportional to the square of the atomic number (Z^2) and to the thickness of the sample. HAADF-STEM imaging is therefore both chemically-sensitive and thickness-dependent. The HAADF-STEM image at low magnification reveals that most of the microspheres have a core-shell yolk-like structure (Figure 1(c)). The X-ray diffraction (XRD) pattern (Figure 1(d)) shows a high crystallinity of the as-synthesized microspheres, with both the rutile and anatase phase present. All diffraction peaks match well with the anatase (A) and rutile (R) TiO_2 (JCPDS cards no. 21-1272 and 12-1276 respectively). However, the exact composition, as well as the phase distribution, are unclear from HAADF-STEM and XRD.
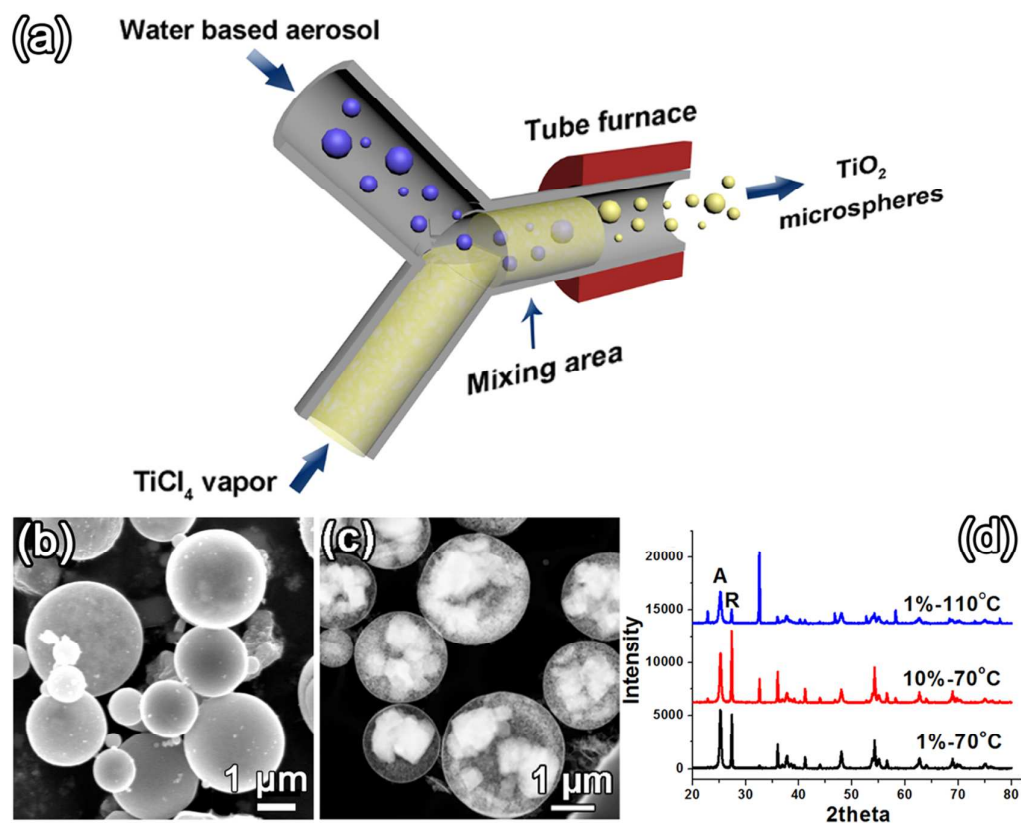
Figure 1. (a) Schematic illustration of the synthesis of the rutile@anatase core-shell structured microspheres; (b, c) SEM and HAADF-STEM images of the sample obtained at 10% urea and $TiCl_4$ at an evaporator temperature of 70 ^{o}C, (d) XRD patterns of the products obtained at different urea concentration and $TiCl_4$ evaporator temperature.

A detailed investigation of the internal microsphere structure by HAADF-STEM (Figure 2(a-d)) reveals the presence of four types of morphologies: yolk structured spheres, foggy-spheres, foam-filled spheres, and hollow spheres, denoted as yolk, foggy, foam, and hollow respectively. Analysis of over 300 microspheres (see Supporting Information Figure S3) leads us to the following relative occurrence: 58% yolk, 8% foggy, 24% foam and 10% hollow. The shell of all microspheres consists of 10-60 nm nanocrystals, while the core of the yolk particles consists of some bigger crystals up to 500 nm. Hollow and foam types possess a thick shell of about 60 - 300 nm while foggy and yolk types have a very thin shell of less than 25 nm (Figure 2(e-h)). Among all these sphere types only the yolk morphology has an apparent core inside the shell. The foggy microspheres might also have some relatively large crystal particles hiding inside the microsphere (indicated in Figure 2(c) by red circles). The corresponding selected area electron diffraction (SAED) patterns in the case of the hollow (Figure 2(i)) and foam-filled (Figure 2(j)) microspheres reveal a pure anatase phase while the SAED pattern of the foggy and yolk microspheres presents some rutile patterns mixed with anatase diffraction rings. (indicated in Figure 2(k,l)). Therefore, the hollow and foam-filled microspheres consist of only the anatase phase, while the foggy and yolk microspheres contain both the rutile and anatase phases in different ratios. The thickness of the shell in microspheres *without* the rutile phase (hollow microsphere: 65nm and foam-filled microsphere: 42nm, indicated in Figure 2 (e) and (f)) is typically much larger than that of the microspheres *with* the rutile phase (foggy microsphere: 16nm and yolk microsphere: 15nm, indicated in Figure 2 (g) and (h)). However, the phase distribution cannot be determined from diffraction or imaging in TEM.
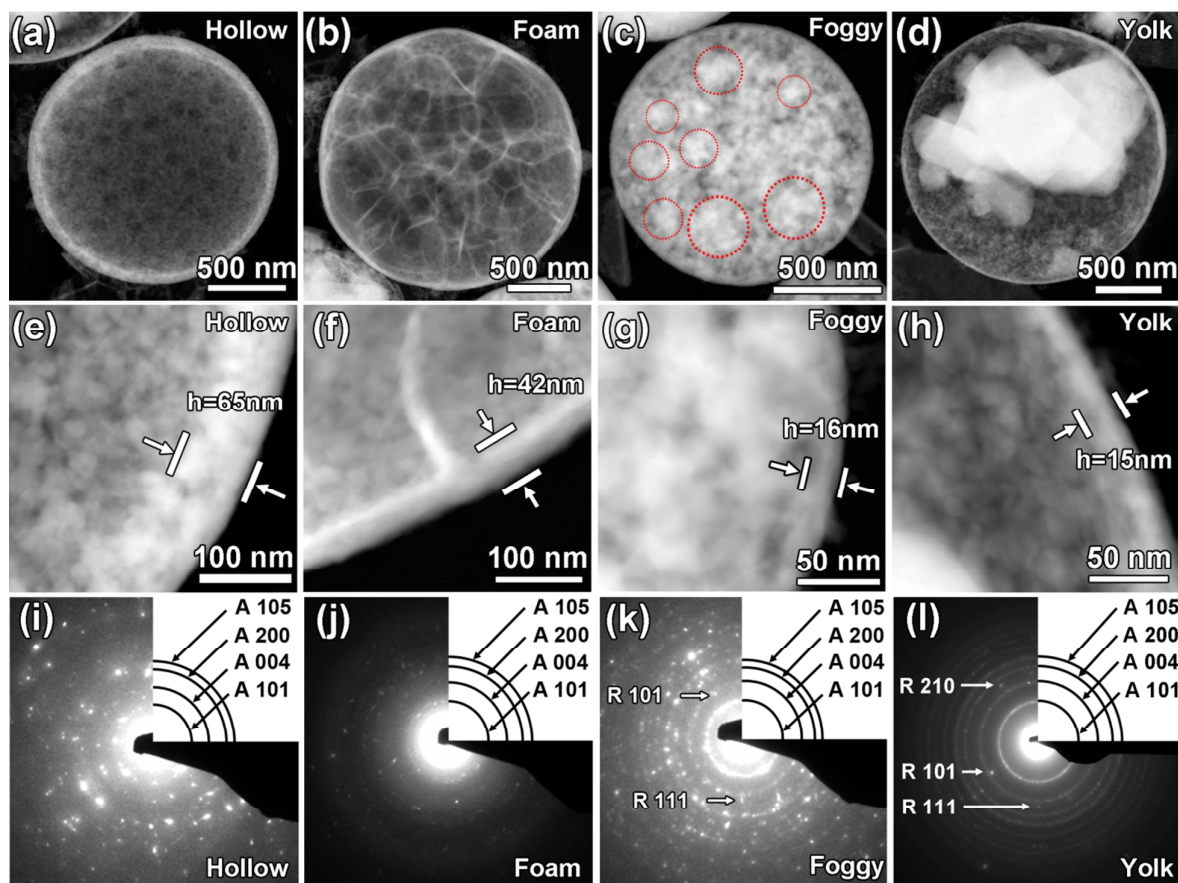
Figure 2. (a-d) HAADF-STEM images of different structures; (e-f) corresponding HAADF-STEM images at higher magnification from the edge of the microspheres; (i-l) corresponding SAED patterns of the whole microspheres in (a-d). Hollow structure is shown in (a, e, and i), foam structure in (b, f, and j), foggy structure in (c, g, and k), and yolk structure in (d, h, and l).

In order to investigate the spatial distribution of anatase and rutile, electron energy-loss spectroscopy has been used to analyze and map the phase distribution. The hybrid structure of rutile/anatase can be diagnosed through high-resolution EELS analysis by focusing on the differences of the Ti $L_{2,3}$ edge between anatase and rutile, which is one of the most reliable ways to distinguish between rutile and anatase on a nanoscale[23,31,32] In the EELS process incident electrons are inelastically scattered on passing through the sample and losing energy. A core electron of the material can be promoted to an unoccupied state, and therefore the

corresponding core edge (the Ti $L_{2,3}$ edge in our case) in the spectrum will carry information about the electronic structure and the symmetry of the corresponding excited atom. This fine structure analysis can be used to identify different components and phases. Furthermore, by using an annular dark-field detector to collect the electrons scattered over large angles, image acquisition and the collection of energy-loss scattered electrons can take place simultaneously. This makes HAADF-STEM-EELS ideally suited for the study of our hybrid rutile@anatase microspheres due to the fact that imaging can be directly combined with local chemical and structural information. The HAADF-STEM image (Figure 3(a)) shows a typical rutile@anatase core-shell microsphere. The corresponding EELS spectra of the Ti $L_{2,3}$ edge from zone 1 and zone 2, indicated in Figure 3(a), are shown in Figure 3(b) (in blue and black respectively). The EELS spectra of the same $L_{2,3}$ edge for pure anatase (red) and pure rutile (green) are also shown in Figure 3(b) as references. All the spectra in Figure 3(b) have been processed under the same conditions, and all treated by background removal and deconvolution. The core-loss EELS Ti $L_{2,3}$ spectra are composed of two groups of peaks associated with L_3 and L_2 transitions. Furthermore, the L_3 and L_2 lines for both phases are initially split into two peaks (L_3: A and B, L_2: C and D). This splitting into the t_{2g} ($3d_\pi$) and e_g ($3d_\sigma$) bands occurs because of the nearly octahedral coordination of Ti in anatase (D2d) and rutile (D2h). Both spectra (anatase and rutile) also show that the L_3 e_g - related peak is further split into two distinct peaks (B_1 and B_2) appearing as a low-energy shoulder for rutile and a high-energy shoulder for anatase. The intensity ratio between these two peaks varies as a function of the TiO_2 crystal structure and is inverted in the case of anatase and rutile. Therefore, the most prominent difference of rutile and anatase is the asymmetrical splitting of the L_3 e_g peak in a high-energy and a low-energy shoulder (Figure 3(b)) indicated by arrows at B_1 and B_2. The spectrum of zone 1 presents a curve (Figure 3(b) blue) similar to the anatase reference (Figure 3(b) red spectrum), implying that the shell is composed by anatase particles. However, the spectrum of zone 2 (Figure 3(b) black) reveals a flat plateau on the L_3 e_g related

peak, which suggests a co-existence of both rutile and anatase. The rutile phase probably comes from the core bulk in zone 2, and the anatase phase comes from the shell part. Because the EELS results are based on 2D imaging in a TEM, the EELS spectrum of zone2 will contain both anatase (top and bottom shell) and rutile information (see Supporting Information Figure S9), however, the pure anatase information can be obtained in Zone1. This implies that in a core@shell configuration pure rutile-core information cannot be observed independently. Hence, the sample has been crushed and a core bulk with clean surface free of shell particles is further used to perform EELS (see Supporting Information Figure S1). Obviously, the core bulk presents a curve (Supporting Information Figure S1) similar to the pure rutile spectrum (Figure 3(b) green spectrum). In order to map the hybrid phases of rutile and anatase, the Ti L_3 e_g peaks in the spectra of every pixel were fitted using the EELSMODEL program (Figure 3(d-f)).[33] According to this program, the fitting and mapping results do not only show a qualitative characterization but provide also quantitative results[33,34]. Further the distribution of rutile and anatase based on the quantification of every pixel in the EELSMODEL program is clearly presented, showing a shell consisting of anatase nanoparticles and a core of rutile bulk. Note that the thick center of the bulk prevents the EELS signal from passing through the very center of the bulk. However, it does not influence the result and conclusion because we can obtain the spectrum on the edge of core bulk and no signal can be detected from both sides of rutile and anatase. Similar EELS maps can be obtained from other samples with separated core and shell (Supporting Information Figure S1 and Figure S2). These EELS mapping results confirm the idea that the core bulk has the rutile structure while the shell nanoparticles are anatase. A similar EELS characterization has been performed on the other types of microspheres (Figure S2). The EELS spectra of the core part of these microspheres (zone1: hollow structure; zone2: foam-filled structure; zone3: foggy structure) demonstrate that the hollow and foam-filled microspheres are purely anatase, while the foggy microsphere consists of a mixture of rutile and anatase because some rutile bulks are buried in the core of the foggy microsphere.

One should not forget that all these characterizations are based on 2D projections of a 3D object. 3D characterization can be achieved through electron tomography, a technique in which several 2D projections are combined into a 3D reconstruction using a mathematical reconstruction algorithm.[35] To obtain a 3D representation of the core-shell structure, HAADF-STEM electron tomography (Figure 3(c) and Video-Tomo in Supporting Information) was carried out on a core-shell type rutile-anatase microsphere (Figure 3(c) inset). The corresponding volume reconstruction (Figure 3(c)) demonstrates a clear core-shell yolk structure, which is made up of a bulk core and a thin shell. To achieve a better visualization of this composite, ortho-slices are shown in Video-Tomo (see Supporting Information). The space between the core and the shell can be easily observed, indicating that the core is isolated from the shell with an ideal yolk structure. In agreement with the EELS study, the bulk inside the microsphere is the rutile phase, green in Figure 3(c), while the anatase phase of the shell is in orange.

The results presented here clearly demonstrate that the microspheres fabricated via heterogeneous $TiCl_4$ vapor hydrolysis show a yolk structure with a rutile core and an anatase shell.
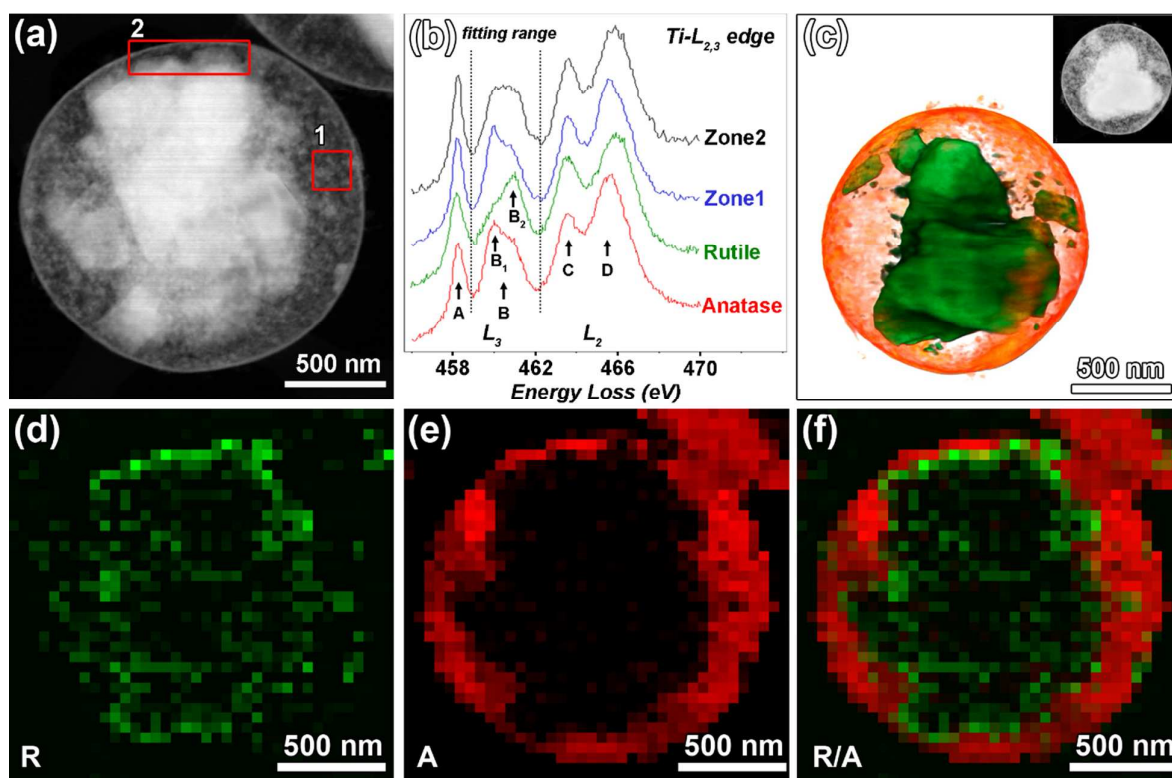
Figure 3. (a) HAADF-STEM image of a typical rutile@anatase core@shell microsphere; (b) Titanium $L_{2,3}$ core-loss EELS spectra acquired from the indicated areas shown in (a) compared to reference TiO_2 polymorphs: rutile (green) and anatase (red) and from the different areas indicated in (a): zone1 (blue) and zone2 (black); (d-f) EELS maps: (d) rutile (green), (e) anatase (red), and (f) rutile and anatase overlaid color map. (c) 3D tomographic reconstruction of another typical rutile@anatase core-shell microsphere, together with the corresponding HAADF-STEM image (inset).

In order to understand the formation mechanism of these different sphere types, we have to consider some basic features of the interaction process between gaseous $TiCl_4$ and water aerosol droplets.

It is known, that $TiCl_4$ reacts intensively with water according to the net reaction:

$$TiCl_{4(gas)} + 2H_2O_{(liquid)} = TiO_{2(solid)} + 4HCl_{(gas)}$$
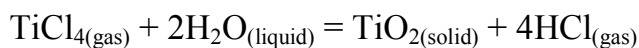
Such a stoichiometric reaction would lead to a 1.8 times decrease in the total volume of condensed substances (36 ml of liquid water would give 20 ml of solid TiO_2). Taking into account that the hydrolysis process starts on the aerosol water-air interface, forming a quasi-solid shell[36], and that then $TiCl_4$ diffuses inside the droplet, the final solid spheres cannot be formed because of a decrease in material volume, thus the resulting microspheres have to be hollow with $V_{shell} = 0.55*V_{sphere}$ and a shell thickness $h_{theor} = 0.12*D_{shell}$ (see SI Figure S6).

Among all the experimentally observed morphology types, only the hollow morphology can be accurately described in terms of sphere diameter (D) and shell thickness (h). The h/D ratio, calculated from the HAADF-STEM images (examples in Figure 2(a-h)), is shown at Figure 4(a).
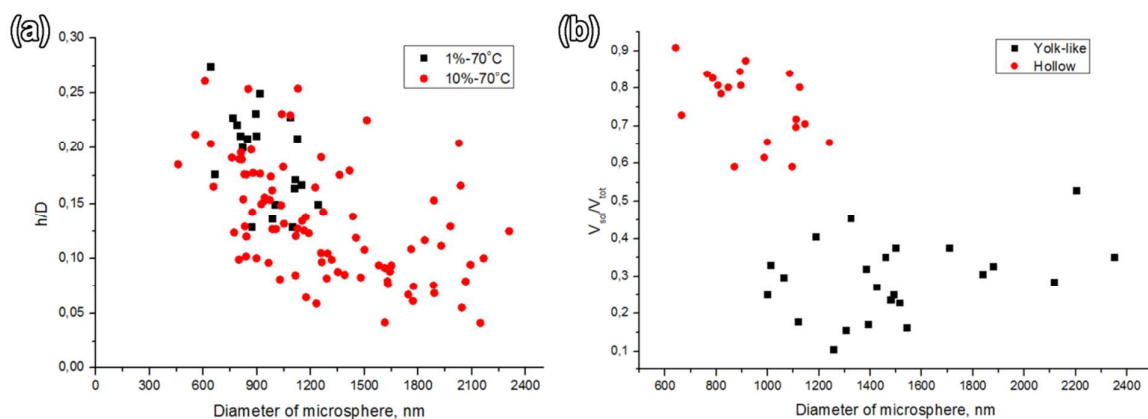

Figure 4. (a) Value of h/D for hollow spheres in samples obtained at urea concentration 1% and 10% and $TiCl_4$ evaporator temperature 70°C; (b) value of V_{solid}/V_{total} for two extreme microsphere's morphologies – hollow and yolk.

The maximum observed h/D value of 0.25 is much higher than the predicted value of 0.12; this is obviously caused by a shrinkage of the spheres during the solid product calcination in the hot furnace zone. To fulfill the h/D increase from 0.12 to 0.25, the final diameter (D_{final}) of the shrunken spheres should be $D_{final}=0.87*D_{initial}$ (see SI Figure S7), which is quite reasonable taking into account the loss of chemically bonded water associated with the heat treatment. Moreover, for most of the hollow spheres, the value of h/D is in between 0.05 and 0.25, so that it can be

concluded that the microsphere formation process, in general, occurs under conditions of $TiCl_4$ deficiency with respect to hydrolyzing solution droplets.

In should be noted, that the T-piece tube connector (Figure 1(a)) used as a mixing unit in synthesis setup gives some inhomogeneity in flow mixing. Together with the inherent polydispersity of the ultrasonic aerosols it would lead to a variable amount of $TiCl_4$ vapor corresponding to each droplet of water aerosol. Therefore, the aerosol droplets can react with a different concentration of $TiCl_4$ vapor in different flow points, resulting in different morphologies.

To corroborate the suggestion of the influence of the $TiCl_4$ vapor concentration on the particle morphology, we calculated the relative value of the solid phase inside the microspheres – V_{solid}/V_{total} - for two extreme morphologies – hollow and yolk –, as shown in Figure 4(b). The volume of the solid phase of the core in yolk particles is estimated (obviously with some overestimation) as the volume of spheres which would have the same maximum cross-sectional area as the area of the core itself.

The V_{solid}/V_{total} value is a merit of the total Ti^{4+} concentration in droplets and reflects the amount of $TiCl_4$ vapor corresponding to a droplet of water aerosol. The V_{solid}/V_{total} value is lower for the yolk spheres than for the hollow spheres, therefore it can be concluded that the yolk spheres are formed at lower $TiCl_4$ concentration than the hollow spheres.

Based on the obtained results, we suggest the following formation mechanism of spheres with a different morphology (Figure 5):

a) A water droplet initially contacts with the $TiCl_4$ vapor and the formation of a thin non-compact shell takes place on the water-air interface;

b) At higher $TiCl_4$ concentrations, $TiCl_4$ diffuses rapidly through the initially formed thin shell inside the sphere, hydrolyses and deposits as $TiO_2 \cdot H_2O$ on the inner surface of the shell, causing the formation of a thicker shell (preformed hollow spheres of $TiO_2 \cdot H_2O$). Coming closer to the hot zone of

the furnace, the preformed hollow spheres lose water and form hollow TiO_2 spheres.

c) At lower $TiCl_4$ concentrations, $TiCl_4$ diffuses slowly through the shell inside the sphere and forms inside the droplets Ti^{4+} aqua complexes stabilized with HCl and urea molecules. Then, the solution of Ti^{4+} aqua complex inside the shell decomposes and forms in the hot zone a rutile core inside the thin shell of the yolk spheres;

d) Hollow and yolk spheres shrink in the furnace about 13% due to the hydrated titania calcination and liberation of water.
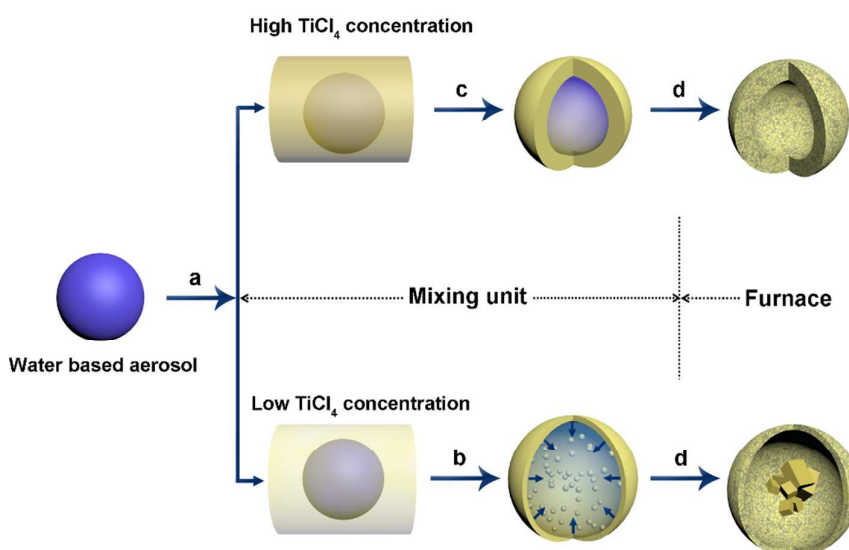

Figure 5. Suggested formation mechanism of spheres with different morphology

The influence of synthesis conditions (urea concentration in hydrolyzing solution and $TiCl_4$ evaporator temperature) on the relative occurrence of yolk spheres in the samples supports the proposed mechanism. A higher $TiCl_4$ evaporation temperature, increased from 70 ^oC to 110 ^oC (meaning an increase of $TiCl_4$ concentration) leads to a decrease of the number of yolk spheres in the sample from 58% to 10% (a counting based on 300 microspheres). A decrease of urea concentration in the hydrolyzing solution from 10 mass.% to 1 mass.% (i.e. lowering the stabilization ability of the acidic solution inside the droplets) leads to

a decrease of the number of yolk spheres from 58% to 23% (a counting based on 300 microspheres). Several HAADF-STEM images of this series of spheres are provided in supporting information (see SI Figure S4 and S5). The foam and foggy morphology types can possibly be explained as a transition state between hollow and yolk morphologies.

The suggested mechanism, featured by $TiCl_4$ templated hydrolysis on the aerosol water-air interface, represents a novel type of heterogeneous transformation accomplishing the known variants of yolk-shell microsphere formation, comprehensively discussed in a review by Liu et al.[37]

3. Conclusions

The new preparation technique introduces a one-step preparation of rutile@anatase core-shell microspheres with the yield around 58% using a simple experimental setup. Advanced TEM characterizations fully corroborate the rutile-core and anatase-shell in the yolk structured microspheres. The water-air interface during the synthesis plays a crucial role in the formation of microspheres with a yolk-shell morphology. A four-point mechanism of a crystalline rutile core formation in a spherical anatase shell is proposed based on a statistical analysis of the HAADF-STEM images. The $TiCl_4$ concentration and urea concentration in the hydrolyzing solution are found to be critical synthesis parameters influencing the yield of yolk spheres. Further engineering of the mixing unit and synthesis conditions are essential to increase the yield of core-shell particles.

4. Experimental section

Methods:

The synthesis experimental setup is described in detail by Tarasov et al.[20] The $TiCl_4$ evaporator with liquid $TiCl_4$ was preheated to 70 ^{o}C - 110 ^{o}C, the dependence of $TiCl_4$ vapor pressure and concentration on temperature are shown on Figure S8. The heating zone of the tube furnace was preheated to 1000°C.

Characterization:

XRD analyzes were performed using a Rigaku D/MAX 2500 diffractometer (Japan) with a rotating copper anode (CuKα irradiation, $5 - 90^{\circ}$ 2θ range, 0.02° step). Diffraction maxima were indexed using the PDF-2 database. The coherent scattering area (CSA) sizes were calculated with the Sherrer equation. The quantitative phase composition of the obtained samples was determined by the normalized Reference Intensity Ratio (RIR) method. The morphology of the samples was studied by scanning electron microscopy Leo Supra 50VP (Germany).

TEM, SAED, and HAADF-STEM were performed on a FEI Tecnai G2 microscope operated at 200kV. STEM-EELS was performed on a FEI Titan 60-300 "cubed" microscope fitted with an aberration-corrector for the probe forming mode, a monochromator, a GIF Quantum energy filter for spectroscopy, operated at 300 kV.

Electron tomography experiments were performed on a FEI Tecnai Osiris microscope equipped with a -70° to +70° tomography tilt stage and holder, operated at 200kV. Images for tomographic reconstruction were taken using a 2° interval, over the largest possible tilting range (preferably 140°). Tomographic reconstruction was performed using the ASTRA Tomography Toolbox.[38]

5. Acknowledgements

5. References

(1)   O'Regan, B.; Grätzel, M. A Low-Cost, High-Efficiency Solar Cell Based on

Dye-Sensitized Colloidal TiO2 Films. *Nature* **1991**, *353* (6346), 737–740.

(2)   Selli, E.; Chiarello, G. L.; Quartarone, E.; Mustarelli, P.; Rossetti, I.; Forni, L. A Photocatalytic Water Splitting Device for Separate Hydrogen and Oxygen Evolution. *Chem. Commun.* **2007**, No. 47, 5022.

(3)   Akira, F.; Kazuhito, H.; Toshiya, W. *TiO2 Photocatalysis: Fundamentals and Applications*; Tokyo Bkc: Tokyo, 1999.

(4)   Ao, C. H.; Lee, S. C. Indoor Air Purification by Photocatalyst TiO2 Immobilized on an Activated Carbon Filter Installed in an Air Cleaner. *Chem. Eng. Sci.* **2005**, *60* (1), 103–109.

(5)   Zhang, G.; Wu, H. Bin; Song, T.; Paik, U.; Lou, X. W. D. TiO2 Hollow Spheres Composed of Highly Crystalline Nanocrystals Exhibit Superior Lithium Storage Properties. *Angew. Chemie Int. Ed.* **2014**, *53* (46), 12590–12593.

(6)   Liu, Z.; Zhang, X.; Nishimoto, S.; Jin, M.; Tryk, D. A.; Murakami, T.; Fujishima, A. Anatase TiO2 Nanoparticles on Rutile TiO2 Nanorods: A Heterogeneous Nanostructure via Layer-by-Layer Assembly. *Langmuir* **2007**, *23* (22), 10916–10919.

(7)   Xie, Y.; Zhang, X.; Ma, P.; Wu, Z.; Piao, L. Hierarchical TiO2 Photocatalysts with a One-Dimensional Heterojunction for Improved Photocatalytic Activities. *Nano Res.* **2015**, *8* (6), 2092–2101.

(8)   Wu, C.; Yue, Y.; Deng, X.; Hua, W.; Gao, Z. Investigation on the Synergetic Effect between Anatase and Rutile Nanoparticles in Gas-Phase Photocatalytic Oxidations. *Catal. Today* **2004**, *93–95*, 863–869.

(9)   Zachariah, A.; Baiju, K. V.; Shukla, S.; Deepa, K. S.; James, J.; Warrier, K. G. K. Synergistic Effect in Photocatalysis As Observed for Mixed-Phase Nanocrystalline Titania Processed via Sol−Gel Solvent Mixing and Calcination. *J. Phys. Chem. C* **2008**, *112* (30), 11345–11356.

(10) Su, R.; Bechstein, R.; Sø, L.; Vang, R. T.; Sillassen, M.; Esbjörnsson, B.; Palmqvist, A.; Besenbacher, F. How the Anatase-to-Rutile Ratio Influences the Photoreactivity of TiO2. *J. Phys. Chem. C* **2011**, *115* (49), 24287–24292.

(11) van der Meulen, T.; Mattson, A.; Österlund, L. A Comparative Study of the Photocatalytic Oxidation of Propane on Anatase, Rutile, and Mixed-Phase Anatase–rutile TiO2 Nanoparticles: Role of Surface Intermediates. *J. Catal.* **2007**, *251* (1), 131–144.

(12) Shi, F.; Li, Y.; Zhang, Q.; Wang, H. Preparation of Core/shell Structured Rutile/anatase Photocatalyst via Vapor Phase Hydrolysis and Its Photocatalytic Degradation of Phenol and Methylene Blue. *J. Am. Ceram. Soc.* **2012**, *95* (6), 1927–1932.

(13) Liu, G.; Yan, X.; Chen, Z.; Wang, X.; Wang, L.; Lu, G. Q.; Cheng, H.-M. Synthesis of Rutile–anatase Core–shell Structured TiO2 for Photocatalysis. *J. Mater. Chem.* **2009**, *19* (36), 6590.

(14) Liu, B.; Khare, A.; Aydil, E. S. TiO2-B/anatase Core-Shell Heterojunction Nanowires for Photocatalysis. *ACS Appl. Mater. Interfaces* **2011**, *3* (11), 4444–4450.

(15) Zhu, Y.; Li, X.; He, G.; Qi, X. Magnetic C–C@Fe3O4 Double-Shelled Hollow Microspheres via Aerosol-Based Fe3O4@C-SiO2 Core–shell Particles. *Chem. Commun.* **2015**, *51* (14), 2991–2994.

(16) Kim, M.; Laine, R. M. One-Step Synthesis of Core−Shell (Ce0.7Zr0.3O2)x(Al2O3)1− x[(Ce0.7Zr0.3O2)@Al2O3] Nanopowders via Liquid-Feed Flame Spray Pyrolysis (LF-FSP). *J. Am. Chem. Soc.* **2009**, *131* (26), 9220–9229.

(17) Basak, S.; Tiwari, V.; Fan, J.; Achilefu, S. Single Step Aerosol Synthesis of Nanocomposites by Aerosol Routes: γ-Fe2O3/SiO2 and Their Functionalization. *J. Mater. Res.* **2011**, *26* (10), 1225–1233.

(18)   Jiang, X.; Brinker, C. J. Aerosol-Assisted Self-Assembly of Single-Crystal Core / Nanoporous Shell Particles as Model Controlled Release Capsules. *J. Am. Chem. Soc.* **2006**, *128* (14), 4512–4513.

(19)   Stopic, S.; Friedrich, B.; Schroeder, M.; Weirich, T. E. Synthesis of TiO2 core/RuO2 Shell Particles Using Multistep Ultrasonic Spray Pyrolysis. *Mater. Res. Bull.* **2013**, *48* (9), 3633–3635.

(20)   Tarasov, A.; Trusov, G.; Minnekhanov, A.; Gil, D.; Konstantinova, E.; Goodilin, E.; Dobrovolsky, Y. Facile Preparation of Nitrogen-Doped Nanostructured Titania Microspheres by a New Method of Thermally Assisted Reactions in Aqueous Sprays. *J. Mater. Chem. A* **2014**, *2* (9), 3102.

(21)   Tarasov, A.; Minnekhanov, A.; Trusov, G.; Konstantinova, E.; Zyubin, A.; Zyubina, T.; Sadovnikov, A.; Dobrovolsky, Y.; Goodilin, E. Shedding Light on Aging of N □ Doped Titania Photocatalysts. **2015**.

(22)   Van Tendeloo, G.; Bals, S.; Van Aert, S.; Verbeeck, J.; Van Dyck, D. Advanced Electron Microscopy for Advanced Materials. *Adv. Mater.* **2012**, *24* (42), 5655–5675.

(23)   Cheynet, M.; Pokrant, S.; Irsen, S.; Krüger, P. New Fine Structures Resolved at the ELNES Ti-L2,3 Edge Spectra of Anatase and Rutile: Comparison between Experiment and Calculation. *Ultramicroscopy* **2010**, *110* (8), 1046–1053.

(24)   Brydson, R.; Sauer, H.; Engel, W.; Thomass, J. M.; Zeitler, E.; Kosugi, N.; Kuroda, H. Electron Energy Loss and X-Ray Absorption Spectroscopy of Rutile and Anatase: A Test of Structural Sensitivity. *J. Phys. Condens. Matter* **1989**, *1* (4), 797–812.

(25)   Bals, S.; Goris, B.; Liz-Marzán, L. M.; Van Tendeloo, G. Three-Dimensional Characterization of Noble-Metal Nanoparticles and Their Assemblies by Electron Tomography. *Angew. Chemie Int. Ed.* **2014**, *53* (40), 10600–10610.

(26) Bals, S.; Van Aert, S.; Van Tendeloo, G. High Resolution Electron Tomography. *Curr. Opin. Solid State Mater. Sci.* **2013**, *17* (3), 107–114.

(27) Midgley, P. A.; Weyland, M. 3D Electron Microscopy in the Physical Sciences: The Development of Z-Contrast and EFTEM Tomography. *Ultramicroscopy* **2003**, *96* (3–4), 413–431.

(28) Midgley, P. A.; Dunin-Borkowski, R. E. Electron Tomography and Holography in Materials Science. *Nat. Mater.* **2009**, *8* (4), 271–280.

(29) Midgley, P. A.; Ward, E. P. W.; Hungría, A. B.; Thomas, J. M. Nanotomography in the Chemical, Biological and Materials Sciences. *Chem. Soc. Rev.* **2007**, *36* (9), 1477.

(30) Ercius, P.; Alaidi, O.; Rames, M. J.; Ren, G. Electron Tomography: A Three-Dimensional Analytic Tool for Hard and Soft Materials Research. *Adv. Mater.* **2015**, *27* (38), 5638–5663.

(31) Lazar, S.; Botton, G. A.; Wu, M.-Y.; Tichelaar, F. D.; Zandbergen, H. W. Materials Science Applications of HREELS in near Edge Structure Analysis and Low-Energy Loss Spectroscopy. *Ultramicroscopy* **2003**, *96* (3–4), 535–546.

(32) Gloter, A.; Ewels, C.; Umek, P.; Arcon, D.; Colliex, C. Electronic Structure of Titania-Based Nanotubes Investigated by EELS Spectroscopy. *Phys. Rev. B* **2009**, *80* (3), 35413.

(33) Verbeeck, J.; Van Aert, S. Model Based Quantification of EELS Spectra. *Ultramicroscopy* **2004**, *101* (2–4), 207–224.

(34) Bertoni, G.; Beyers, E.; Verbeeck, J.; Mertens, M.; Cool, P.; Vansant, E. F.; Van Tendeloo, G. Quantification of Crystalline and Amorphous Content in Porous Samples from Electron Energy Loss Spectroscopy. *Ultramicroscopy* **2006**, *106* (7), 630–635.

(35) Goris, B.; Roelandts, T.; Batenburg, K. J.; Heidari Mezerji, H.; Bals, S.

Advanced Reconstruction Algorithms for Electron Tomography: From Comparison to Combination. *Ultramicroscopy* **2013**, *127*, 40–47.

(36) Tarasov, A. B.; Trusov, G. V.; Gruzinov, A. Y.; Goodilin, E. A.; Zabelin, A. V. Investigation of Interactions of Gaseous Titanium Tetrachloride with Water Aerosol by in-Situ Small Angle X-Ray Scattering Using Synchrotron Irradiation. *Nanosyst. PHYSICS, Chem. Math.* **2013**, *4* (1), 139–147.

(37) Liu, J.; Qiao, S. Z.; Chen, J. S.; (David) Lou, X. W.; Xing, X.; (Max) Lu, G. Q. Yolk/shell Nanoparticles: New Platforms for Nanoreactors, Drug Delivery and Lithium-Ion Batteries. *Chem. Commun.* **2011**, *47*, 12578–12591.

(38) van Aarle, W.; Palenstijn, W. J.; De Beenhouwer, J.; Altantzis, T.; Bals, S.; Batenburg, K. J.; Sijbers, J. The ASTRA Toolbox: A Platform for Advanced Algorithm Development in Electron Tomography. *Ultramicroscopy* **2015**, *157*, 35–47.

For Table of Contents only